

Contents lists available at ScienceDirect

Displays

journal homepage: www.elsevier.com/locate/displa





Design of large-angle distortion-free and spot adjustable LED spot array projector based on microlens array and eyepiece[★]

Yue Liu^a, Jingping Zhu^{a,*}, Chen Chen^b, Xun Hou^a

- ^a Key Laboratory for Physical Electronics and Devices of the Ministry of Education and Shaanxi Key Laboratory of Information Photonic Technique, Xi'an Jiaotong University, Xi'an 710049, China
- ^b Shang Hai OE Technology Co., LTD, Putuo District, Shanghai 200333, China

ARTICLE INFO

Keywords: Spot array projector Microlens arrays Optimization method Radial basis function Distortion

ABSTRACT

The spot array projector has long been a challenging and intriguing research focus in the fields of projection and lighting applications. In the current literature, there is a lack of a comprehensive and detailed presentation on the design and analysis method for a spot array generator based on the structure of imaging eyepiece and MLA. We present a novel design and optimization method for a large-angle, distortion-free and spot adjustable LED spot array projector that is composed of an eyepiece, two microlens arrays (MLAs), and a micro-LED array (MLEDA). The eyepiece system is optimized using imaging optical methods to project sub-beams to the target plane with a large angle. The sub-lens of condenser MLA is also optimized using imaging optical methods to refocus the collimating beam and match the numerical aperture (NA) with the eyepiece, and the sub-lens of the collimating MLA is acquired by using simulated annealing (SA) global illumination optics optimization method to achieve collimation and far-field homogenization. The predistortion MLEDA and the MLAs are proposed and implemented by the radial basis function (RBF) interpolation method, which correct the large-angle distortion introduced by the eyepiece. Both near-field and far-field applications can be realized by the proposed system. In the near-field applications, different spot geometries at the near-field target plane can be achieved. In the farfield applications, the power matching of the MLEDA is used to improve far-field uniformity of spot array. Moreover, the predefined-geometry arrangement spot array can be realized in both near and far fields. Two design examples with full field of view (FOV) projection of 80° and 100° are provided to validate the proposed method. Overall, the proposed system offers a promising solution for various applications requiring target identification or 3D calibration.

1. Introduction

The beam splitter, also known as a spot array projector, plays an important role in the fields of beam parallel processing, medical cosmetology, optical detection and projection, optical communication, and structured light lighting [1–3]. The spot array projector based on diffractive optical elements (DOE), or diffraction gratings, is commonly used to achieve beam splitting [4]. The beam splitting DOE, designed based on scalar diffraction theory, diffracts the beam energy into specified diffraction orders and generates an array of sub-beams. However, the beam splitter based on DOE is difficult to achieve the uniform-intensity, low-stray-light, and large-angle spot array projection.

Because large-angle diffraction often requires finer microstructures in DOE, it usually increases the difficulty of the manufacturability. In addition, the need of uniformity projection decreases the diffraction efficiency of the DOE.

Spot array generators based on the refraction principles and the refraction optics have emerged. They have the advantages of relatively high efficiency, high threshold, wavelength insensitivity, and low cost. Jarczynski et al. [5] designed a monolithic multi-facet beam splitter generating a one-dimensional spot array. The entrance surface is described by a cylinder and each exit surface is the optimized XY polynomial freeform surface. Maksimovic et al. [6] proposed an optimization design method for a freeform beam splitter. The entrance

E-mail address: jpzhu@xjtu.edu.cn (J. Zhu).

Abbreviations: MLAs, microlens arrays; MLEDA, micro-LED array; SA, simulated annealing; RBF, radial basis function; NA, numerical aperture; FOV, field of view.

 $^{^{\}star}\,$ This paper was recommended for publication by Prof Guangtao Zhai.

^{*} Corresponding author.

surface of the proposed splitter functions as a collimator and the exit surface converts the collimated beam into multiple converging subbeams. Jia et al. [7] designed a freeform-based splitter for generating identical sub-beams from a given input beam while reducing the influences of diffractions. However, the above freeform-based beam splitters all contain freeform optical elements with complex surface shapes, so it is difficult to ensure the accuracy of the surface shape in the actual fabrication. In addition, the number and arrangement of the generated spot arrays is limited due to the limitations of geometrical element aperture and fabrication.

MLA is also a common geometric optical element used for beam splitting, and its basic principle is to generate a spot array based on pupil segmentation [8]. Owing to the advanced MLA processing technology [9–13], many commercial products for imaging systems have emerged, such as integral display, compound eye imaging, and light-field imaging [14–19]. In addition, MLA exhibits multi-micro-aperture characteristics and has been widely used for illumination owing to their robust beam splitting and light homogenization abilities [20–26]. Compared with the traditional single-aperture lens, MLA shows more compact and lightweight. The spot array generator is responsible for producing an array distribution of light spots on a target surface. This can be achieved using a projector system that combines imaging and illumination systems. However, in the current literature on spot array generators, there is no complete and detailed presentation of the design and analysis method for a spot array generator based on an imaging eyepiece and MLA structure. Eyepieces are commonly used in various imaging systems, including microscopes, telescopes, and popular augmented reality (AR), virtual reality (VR) near-eye display systems [27-31].

In this paper, we propose a novel design and optimization method for a large-angle, distortion-free and spot adjustable LED spot array projector that is composed of an eyepiece, two MLAs, and a MLEDA. An imaging optical optimization method is used to obtain a compact and large-angle eyepiece system. The condenser MLA is also acquired using imaging optical optimization, and it refocuses the collimating beam while matching the numerical aperture (NA) with the eyepiece. The collimating MLA is acquired through Simulated Annealing (SA) optimization method [32-35], and it homogenizes the MLEDA beam for farfield projection. The RBF interpolation method [36] is used to predefine the arrangements of the MLEDA and the sub-lens on the two MLAs, which can correct the large-angle distortion introduced by the eyepiece. Both near-field and far-field applications can be realized by the proposed system. In the near field, different spot geometries at the target plane can be realized by adjusting the opening geometry of the eyepiece diaphragm. In the far-field, power matching of the MLEDA is used to achieve far-field spot array uniformity. The predefined-geometry arrangement of spot array can also be realized in both near and far fields. In addition, comparing to the DOE and freeform-based spot array generators [4-7], the proposed spot array projector only uses spheric and aspheric surfaces, which are currently mature in application and production, resulting in higher stability and lower process sensitivity [9–12,27], and it also has the advantages such as: without central-FOV peak spot, more uniform, free of large-angle distortion and stray-light suppression. Design examples based on two types of eyepieces are given: the first structure is based on the eyepiece structure of the classic Zeiss Astroplan eyepiece [37], which realized a full-FOV projection of 80° and an exit pipul diameter (EPD) of 4.0 mm. The second one is based on a Fresnel lens with a planar base which realized a full-FOV projection of 100° and an EPD of 4.5 mm.

This paper will be developed as follows: The basic principle of the proposed LED spot array projector is detailed in section 2. The detailed design and optimization methods and the design examples of the LED spot array projector are illustrated in section 3. The simulations and analysis of the designed LED spot array projectors are conducted in section 4.

2. Basic principle of LED spot array generator

The basic principle and 3D structure of the proposed LED spot array projector are shown in Fig. 1. The collimating system is an aspheric collimating MLA consisting of discrete-arrangement identical sub-lens with a focal length f_{c1} , which collimates the light from MLEDA. The condenser system is a condenser MLA consisting of the discretearrangement identical sub-lens with focal length f_{c2} . The sub-lenses on the collimating and condenser MLAs all have the same sub-aperture size $r_{\rm s}$ and arrangement positions. The lambertian light comes from MLEDA is collimated by the collimating MLA, and then the discrete and collimated sub-beams are converged to the discrete spots with a converged angle φ_s by the condenser MLA. The discrete spots at the eyepiece image plane (EIP) are projected to the target plane through the eyepiece system. The imaging eyepiece with the aperture size of D_e and the focal length of f_e collimates the light from light points at EIP and emits it at different angles: in the eyepiece system, each sub-beam emits from the light spot at the EIP, diverged, and refracted (or reflected in reflect-type evepiece system) by the evepiece lens, and finally emits out from the adjustable diaphragm of EPD. Since MLED usually has a large divergence angle (half divergence angle $> 50^{\circ}$), it is difficult to achieve the collimation of sub-beam, the concentration of sub-beam at a specific convergence angle, and the function of homogenization through a single MLA. Therefore, a collimating MLA and a condenser MLA were optimized in this paper to achieve the above functions. Ideally, all the discrete sub-beams are emitted as parallel sub-beams from the adjustable diaphragm and the spot array distribution is formed on the target plane at $L_{\rm p}$. The proposed spot-array projector can be used in both nearfield and far-field situations: in the near-field situation ($L_p < 500$ mm), the opening geometry of the eyepiece diaphragm plays a role as an apodization aperture. Therefore, adjustable opening geometry of the eyepiece diaphragm can be used to achieve different spot geometry (size and shape) at the near-filed target plane. In the far-field situation $(L_p \gg 500 \text{ mm})$, the intensity and uniformity of the spot array distribution should be given priority and guaranteed, and the spot geometry is always neglected.

As shown in Fig. 1, assuming the eyepiece lens and sub-lens of two MLAs are ideal thin lenses, which means it would not suffer the distortion and other imaging aberrations in the system (For convenient description, only three sub-beams are shown in the optical path). Then, the relation between the n-th light spot at EIP with a height of h_n and the projection FOV θ_n of the emitted parallel sub-beam from the adjustable diaphragm will be satisfied with:

$$h_n = f_e \tan \theta_n \tag{1}$$

where h_n can be thought of as the Gaussian image height or ideal paraxial image height. The opening size *EPD* of the diaphragm can be expressed by:

$$EPD = 2f_{\rm e} \tan\left(\frac{\varphi_{\rm e}}{2}\right) \approx f_{\rm e} \varphi_{\rm e} \tag{2}$$

where $\varphi_{\rm e}$ is the diverging angle of the spot at the EIP and it is determined by the eyepiece system. The opening size *EPD* of the diaphragm is also the diameter of the projection spot at the target plane. According to the principle of paraxial optical imaging, the total length $L_{\rm s}$ of the system can be approximately expressed by:

$$\begin{cases}
L_{\rm s} = L_{\rm c} + L_{\rm e} \\
L_{\rm c} = f_{\rm c1} + L_{\rm c1} + f_{\rm c2} \\
L_{\rm e} = f_{\rm e} + \frac{D_{\rm e}}{2\tan\theta_{\rm max}}
\end{cases}$$
(3)

where $L_{\rm c}$ and $L_{\rm e}$ are corresponding to the length of the collimating-condenser system and the eyepiece system.

As shown in Fig. 1, to achieve low-loss energy transmission between the collimating and condenser system and the eyepiece system, it should

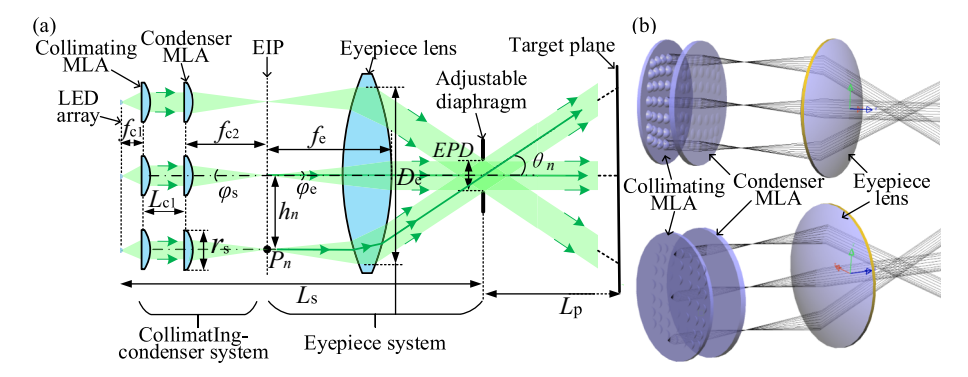


Fig. 1. Basic principle of proposed LED spot array generator. (a) Illustration of basic optical path; (b) 3D view of basic optical structure.

meet the equality of the NA or the beam etendue on both sides of the EIP, namely, meet:

$$\varphi_{\rm e} = \varphi_{\rm s} \tag{4}$$

However, the Eqs. (1–4) are only realized in an ideal or paraxial situation. The following problems need to be considered in the actual situation:

- (1) The quality problem of the individual spot at the target plane. As shown in Fig. 1, when the microlens of condenser MLA converge the sub-beam to the spot P_n on the EIP, the aberrations of the condenser MLA and the eyepiece system will affect the collimation of the sub-beam exiting from the diaphragm (with an exit angle θ_n). It will further cause the size and geometry errors of each individual projected spot, and the illumination uniformity inside each individual projected spot also decreased at the target plane. Furthermore, collimated sub-beam generated by the collimating sub-lens will also make influence on the illumination distribution uniformity of the projected individual spot.
- (2) The illumination nonuniformity problem of the overall spot array at the target plane. For an ideal paraxial eyepiece system, to realize the illumination uniformity of each spot projected at different FOV, only the same energy of each spot at the EIP is required. However, the design of large-FOV eyepieces often deviates significantly from ideal imaging conditions. The nonuniformity reasons in an imaging system are complex and it is determined by: (a) the \cos^3 law, (b) distortion of the entrance pupil at high obliquities, and (c) image distortion. The effects of these various factors have been discussed elsewhere [38]. To meet the illumination uniformity of the projected spots at different FOV, the illumination requirements for the spot P_n at the EIP corresponding to each FOV sub-beam may be different.
- (3) The distortion aberration problem that appeared in the large-FOV eyepiece [39]. To achieve a large-angle projection of the spot array, the large-angle evepiece always has a large distortion aberration. As shown in Fig. 2, the distortion is considered negative when the actual image is closer to the axis than the ideal image, and the positive distortion is the converse. As shown in Fig. 2(a), the ideal imaging point P is distorted to point Q with radial distortion δh . This physically means that the image of a square suffering negative distortion will take on a barrel-like appearance and is referred to as barrel distortion ($\delta h < 0$). As shown in Fig. 2 (b), in the case of positive distortion, the image takes on a pincushion-like appearance and is referred to as pincushion distortion ($\delta h > 0$). In this paper, the EIP of eyepiece always suffers the radial negative (barrel-like) distortion as shown in Fig. 2(a). When the EIP distortion is considered, that is, when the condenser MLA generates an equally-spaced spot array on the EIP, the sub-beam array will emit out from the diaphragm and a non-equally spaced and positive-distortion arrangement of spot

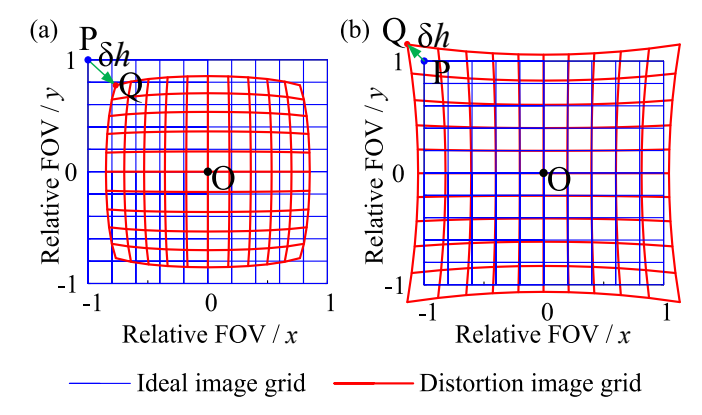


Fig. 2. Image distortion grids. (a) negative and (b)positive radial distortion grids.

array is formed at the target plane. Therefore, the distribution of the spot array at the EIP should be predistorted, which means the spot array at the EIP should be arranged as the reverse distortion, so that the spot array projected at the target plane will be a regular equal-spaced or predefined geometry distribution.

Considering the above-mentioned problems, we will mainly carry out the design in the following parts: For problems (1) and (2), the design of the eyepiece system and the sub-lens of the collimating and condenser MLAs are realized by combining the imaging and illumination system optimization methods; For the problem (3), the predistortion arrangement of the MLEDA and the two MLAs are conducted by using the chief ray tracing and the RBF interpolation method. In the next section, the optimization and design process are detailed.

3. Design method of the spot array generator

Fig. 3 shows the design flow chart of the proposed LED spot array projector herein. The design procedures involved are as follows:

- (a) Selection of the initial eyepiece structure. The potential of achieving large-angle projection, uniformity illumination at EIP, and compactness should be given priority for the selection of the initial eyepiece structure. In this paper, two design examples are proposed, the first initial eyepiece structure is inspired by the classic Zeiss Astroplan eyepiece. The second example is inspired by the classic VR system which is based on a Fresnel lens with a planar base and equal-depth zigzag microstructure.
- (b) $\theta_{n+1} = \theta_n + \delta\theta$. After the selection of the initial eyepiece system, we need to consider if the projection angle is large enough. The projection FOV can be enlarged gradually until the large-angle projection is realized during the multiple optimization loop.

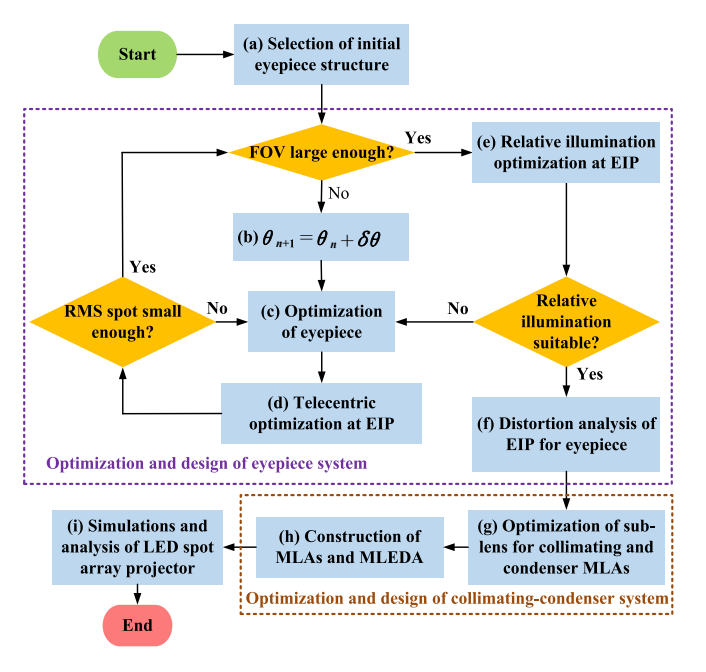


Fig. 3. Design flow chart of proposed LED spot array projector.

- (c) Optimization of the eyepiece. The eyepiece is optimized in a reverse direction, and the imaging points at the EIP are formed by the parallel light entering the pupil of the eyepiece with different FOVs. The eyepiece is optimized by changing the structure and surface profile parameters of the eyepiece system. The merit functions are the RMS spot size and the maximum diverging angle $\varphi_{\rm e}$ of each projection FOV at the EIP. The detailed optimization and analysis procedures are given in section 3.1
- (d) Telecentric optimization at EIP. As depicted in Eq. (4), in order to achieve the equivalence of NA on both sides of EIP and match with the telecentric convergence sub- beams generated by the condenser MLA, the chief ray (the dark green solid line in Fig. 1) of each FOV sub-beam is constrained to be perpendicular to the EIP (telecentric at EIP).
- (e) Relative illumination optimization at the EIP. When the relative illumination of each FOV varies too much or irregular at the EIP, the energy requirement for each MLED is more complex. Therefore, the relative illumination of the eyepiece system is optimized until the relative illumination varies little or smooth monotonic variation from central FOV to edge FOV.
- (f) Distortion analysis of EIP for the eyepiece. The distortion coordinates for each FOV spot at the EIP can be acquired by the chief-ray tracing and RBF interpolation methods which are detailed in section 3.2.
- (g) Optimization of sub-lens for collimating and condenser MLAs. The surface profile parameters optimization of the sub-lens for collimating and condenser MLAs is conducted by imaging and illumination system optimization methods. The merit functions of the collimating sub-lens are the RMS spot size, collimation, and illumination uniformity while the condenser MLA are the RMS spot size and the maximum converging angle φ_s which matches the numerical aperture (NA) of eyepiece at the EIP.
- (h) Construction of MLAs and MLEDA. The collimating and condenser MLAs can be constructed by the thickness of bases, the optimized surfaces, and the predistortion arrangement positions of each sub-lens. The arrangement of the MLEDs is identical to the two MLAs.
- Simulations and analysis of LED spot array projector. Since it is a lighting optical application, the non-sequential ray tracing is used

to analyze and evaluate the final quality of the spot array. The detailed simulations and analysis are given in section 4.

3.1. Optimization and design of eyepiece system

In this section, two eyepiece design examples are given, the first eyepiece is inspired by the structure of the Zeiss Astroplan eyepiece [37], and the initial structure can be obtained in the lens library of the optical design software ZEMAX or CODEV. The 2D and 3D optical structure of optimization results are shown in Fig. 4(a) and Fig. 4(b), the two doublets in the initial structure are changed to singlets due to the illumination application (the polychromatic aberrations are ignored). Lens 1 and Lens 3 are normal spheric glass lenses. Lens 2 is an aspherical lens with PMMA (polymethyl methacrylate) material and the 3D view is shown in Fig. 4(c). The usage of an aspheric surface here can realize a large-angle light deflection and reduction of the aberration. The aspheric surface can be expressed as:

$$z = \frac{cr^2}{1 + \sqrt{1 - (1 + k)c^2r^2}} + \sum_{i=2}^{n} a_{2i}r^{2i}$$
 (5)

The optimized surface profiles of S4 and S5 are analyzed in Fig. 4(d) and Fig. 4(e) which show smooth surface profiles are realized in the optimized aspheric lens. The following design and analysis are conducted at the wavelength of 580 nm. The optimized eyepiece realized a full FOV of 80°, EPD=4 mm, and $f_e=14.99$ mm, and the maximum distortion rate is 25% at the edge FOV. A total length L_e of 41.14 mm from S1 to S8 is realized. The distortion in the optimization process is not controlled, because the distortion problem will be solved by the following design of the MLA. The imaging RMS spot at the EIP (S8) is analyzed. The smaller spot size results in a higher quality light spot at the target plane. As shown in Fig. 4(g), the RMS spot sizes are analyzed for some sampled FOVs of the optimized eyepiece. The main structure and telecentric constraints in CODE V during the optimization process can be expressed by:

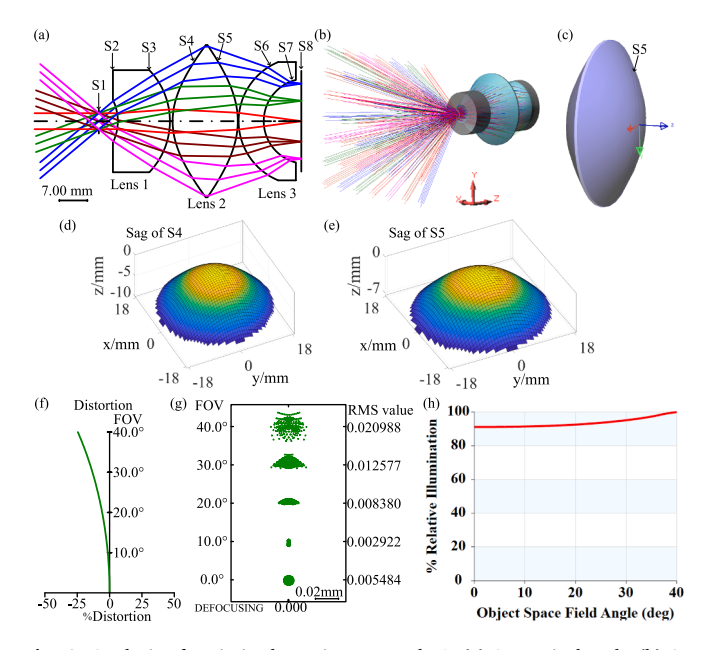


Fig. 4. Analysis of optimized eyepiece example 1. (a) 2D optical path; (b) 3D optical path; (c) the PMMA aspheric lens; (d) sag analysis of S4; (e) sag analysis of S5; (f) distortion curve diagram; (g) RMS spot diagram; (h) relative illumination diagram.

Y FL R1 S8
$$<=$$
 Ymax
OAL S1..8 $<=$ Lmax
K S4 $>$ -5 $<$ 5
K S5 $>$ -5 $<$ 5
AOI R1 S8 F1 = 0
AOI R1 S8 F2 = 0
...

AOI R1 S8 FL = 0

where the first constraint is the maximum actual imaging height Ymax at the EIP (S8). The second constraint is the total length Lmax of the eyepiece system from surface S1 to S8. The third and fourth constraints are used to control the conic parameters for the two aspheric surfaces of S4 and S5 in a suitable bent state. The other constraints are used to control the chief ray (R1) for each FOV (from central FOV F1 to the largest FOV FL) to be vertical to the surface S8, which is also the constraint for realizing the telecentric imaging at the EIP.

Furthermore, by referring to the relative illumination of the projection plane [40], the optimization constraint of relative illumination in CODE V can be expressed as:

where M0 is cosine angle of the central-FOV (F1) up-edge ray (R2) corresponding to y axis (M) at surface S8. M2 is the cosine angle of the largest-FOV (FL) upper-edge ray (R2) corresponding to the y axis (M) at surface S8. M3 is the cosine angle of the largest FOV (FL) right-edge ray (R3) corresponding to the y axis (M) at surface S8. L4 is the cosine angle of the largest-FOV (FL) lower-edge ray (R4) corresponding to \times axis (L) at surface S8. RI is the approximate relative illumination of edge FOV. The final optimized relative illumination of the eyepiece system is shown in Fig. 4(h). The structure and surface parameters of the optimized eyepiece are shown in Table 1.

As shown in Fig. 5, the eyepiece example 2 is designed based on a Fresnel lens with a planar base which realized a full-FOV projection of 100° and $f_{\rm eyepiece} = 18.7$ mm. The planar-based Fresnel lens with a aspheric zigzag surface has an equal depth of 0.3 mm which is suitable for manufacture by injection molding [13]. The optimization process can be also conducted under the constraints of Eqs. (6) and (7) (Only the surface number and FOV are changed). As shown in Fig. 5(a), a diaphragm with an adjustable opening aperture of $0 \sim 4.5$ mm at surface S1 is realized. The 3D structure is shown in Fig. 5(b), and the 3D structure of the aspheric-Fresnel lens is shown in Fig. 5(c). A total length of the eyepiece from S1 to S6 $L_{\rm eyepiece} = 49.5$ mm is realized. Both Lens 1 and Lens 2 are designed with the material of PMMA. Surfaces S2 and S4 are conic surfaces. Surface S3 is the aspheric surface and S5 is the Fresnel surface with the planar base. The optimized surface profiles of S2, S3, and S4 are analyzed in Fig. 5(d-f) which reflect smooth surface profiles

Table 1The coefficients of the optimized eyepiece example 1.

Surface	Y Radius	Thickness	Materials
S1	infinite	4.7329	
S2	-12.2194	13.0000	HZF6_CDGM
S3	-18.4009	0.6782	
S4	17.8397	16.2651	PMMA_SPECIAL
S5	-19.9639	0.2000	
S6	16.0000	6.2690	HK50_CDGM
S7	10.6338	9.3984	

The aspheric parameters used in S4 and S5.

S4: K = -2.0278.

S5: K = 2.2766; a4 = -4.4018e-06; a6 = 5.7731e-09;

a8 = 5.6762e-12; a10 = -1.2901e-14e-11.

are realized. The optimized Fresnel surface profiles of S5 are shown in Fig. 5(g) which shows a smooth surface profile is realized in the zigzag microstructure. The width of the zigzag keeps large enough (nearly 0.28 mm) at the edge of the Fresnel surface which will benefit the manufacture. As shown in Fig. 5(h), the maximum distortion rate is 25% at FOV $=50^{\circ}$. The distortion in the optimization process is also not controlled, because the distortion problem will be solved by the following design of the MLA. The RMS spot diagram analysis is shown in Fig. 5(i). The final optimized relative illumination of the eyepiece system is shown in Fig. 5(j). The structure and surface parameters of the optimized Fresnel-based eyepiece are shown in Table 2.

3.2. Design of condenser MLA with the functionality of predistortion

The design of condenser MLA will mainly be decomposed into two parts: (1) the calculation of predistortion coordinates (the arrangement coordinates of the condenser sub-lens) at the EIP; (2) the optimization of the condenser sub-lens.

(1) The calculation of predistortion coordinates at the EIP. When the eyepiece distortion is considered, a predistortion arrangement of sublens in MLA will help to generate the predefined spot array at the target plane free of distortion. The required coordinates can be obtained by the predistortion calculation method through the known ideal image height grid points and the traced distortion grid points at the EIP. As shown in Fig. 6(a), a calculation process of the predistortion coordinates is given, which requires initial chief-ray tracing to determine the basic mapping relationship, and the RBF interpolation method is used to generate the predistortion point coordinates when a new set of projection spot array FOVs are given. When the new set of spot array FOVs are defined, there is no need to repeat the process of chief-ray tracing which also benefit the engineer without prior knowledge of optical design.

As shown in Fig. 6(b), for a common rectangular arrangement, the projection spot array (x_t, y_t) at the target plane of L_t is generated. θ_x and θ_y are used to predefine the spot projection FOV in the x and y directions:

$$\begin{cases} \theta_{x} = \arctan\left(\frac{x_{t}}{L_{t}}\right) \\ \theta_{y} = \arctan\left(\frac{y_{t}}{L_{t}}\right) \end{cases}$$
(8)

By tracing the chief rays corresponding to the FOVs (θ_x, θ_y) of these spots, the pre-distorted spot-array coordinates at the EIP can be obtained. The coordinates corresponding to each sub-lens on the collimating and condenser MLA is identical to the spot-array coordinates at the EIP.

As shown in Fig. 6(c) and Fig. 6(d), the initial mapping relations corresponding to the eyepiece example 1 and example 2 are established (The blue and red points are corresponding to the initial ideal imaging grid points and the chief ray tracing predistortion grid points). The RBF interpolation method uses n polynomial basis functions (the number of corresponding points is equal to the number of basis functions). Each original regular ideal point M_j (x_j , y_j), and the corresponding ray-tracing points of chief rays $M_j(x_j, y_j)$ can be described as:

$$x'_{j} = \sum_{i=1}^{n} \alpha_{x,i} R_{i}(d) + p_{m}(x_{j}, y_{j})$$
 (9)

$$y'_{j} = \sum_{i=1}^{n} \alpha_{y,i} R_{i}(d) + p_{m}(x_{j}, y_{j})$$
 (10)

$$R_i(d) = \left(d^2 + \lambda r_i^2\right)^{\mu/2} = \left[\left(x_j - x_{\text{center}_i}\right)^2 + \left(y_j - y_{\text{center}_i}\right)^2 + \lambda r_i^2\right]^{\mu/2}$$
 (11)

where R_i represents the i^{th} basis function, centered at $(x_{center_i}, y_{center_i})$, $\alpha_{xy, i}$ are the weights of the basis functions; $p_m(x_j, y_j)$ is a fitting polynomial of order m to guarantee the fitting accuracy of degree m, j is an integer from 1 to n, and λ is a scaling factor. The basis centers are

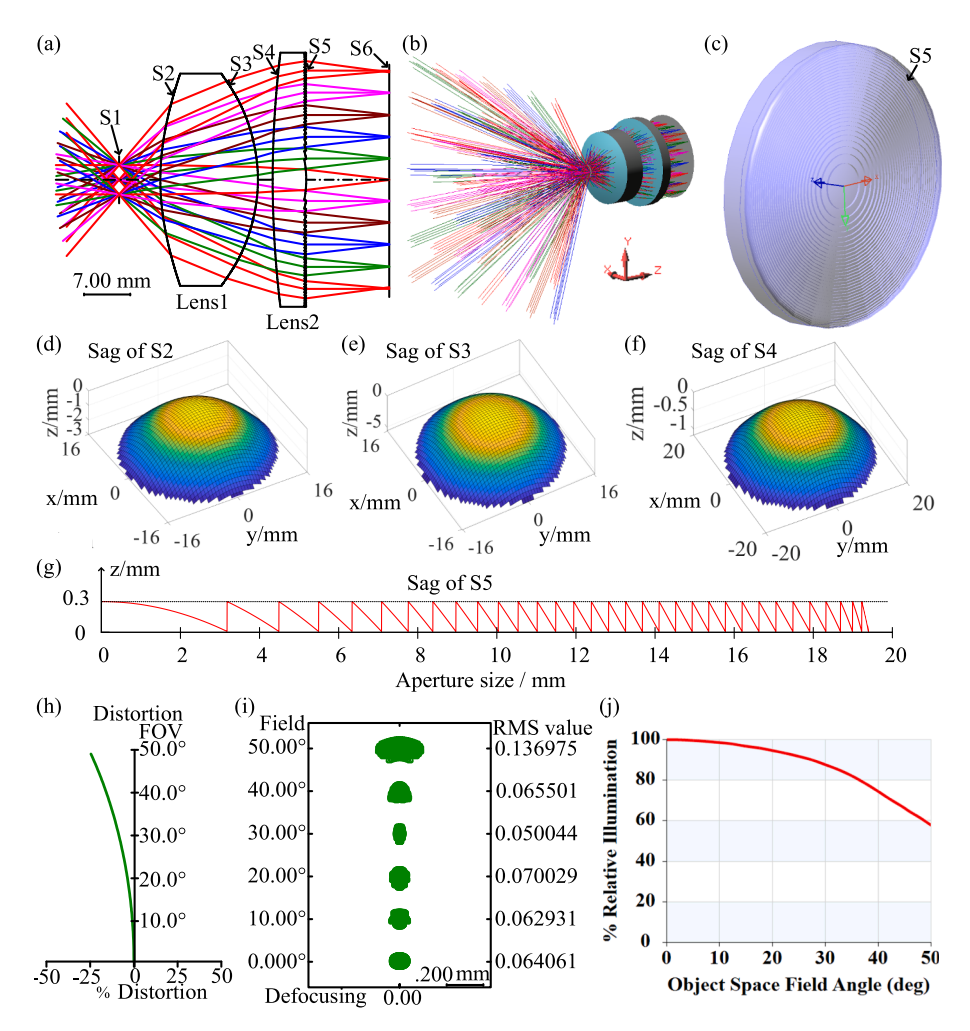


Fig. 5. Analysis of optimized eyepiece example 2. (a) 2D optical path; (b) 3D optical path; (c) 3D PMMA aspheric-Fresnel lens; (d) sag analysis of S2; (e) sag analysis of S3; (f) sag analysis of S4; (g) sag analysis of S5; (f) distortion curve diagram; (g) RMS spot diagram; (h) relative illumination diagram.

Table 2The coefficients of optimized Fresnel-based eyepiece example 2.

Surface	Y Radius	Thickness	Materials
S1	infinite	6.2500	
S2	38.7676	14.7758	PMMA_SPECIAL
S3	-24.4378	2.2320	
S4	160.9488	5.0795	PMMA_SPECIAL
S5	-16.6903	12.5718	

The conic and aspheric parameters used in S3-S6.

S2: K = -4.7127.

S3: K = -0.3711; a4 = 3.2485e-05; a6 = -2.2869e-07;

a8 = 5.1899e-08; a10 = -1.8527e-10.

S4: K = -5.0.

S5: K = -5.0; a4 = 9.0039e-06; a6 = 1.1247e-07;

a8 = -5.0594e-011; a10 = 2.7290e-13.

located at the position of the original grid FOV (blue points), and the characteristic radius r_i is equal to the minimum distance between all the original grid FOV points; furthermore, $\mu = -2$.

In fact, for any designated spot array coordinates (x_t, y_t) or (θ_x, θ_y) , the high-precision predistortion coordinates can be acquired here through the fitting parameters acquired in Eqs. (9–11). Therefore, when the new arrangement positions of the sub-lens need to be calculated, the extra chief-ray tracing process is not required which will benefit the designer who has no prior knowledge of optics. In the simulations of section 4.3, the projection distribution of spot arrays with different

patterns can be realized by the arrangement coordinates acquired by the RBF method.

(2) The surface optimization of the sub-lens in condenser MLA should be conducted. As shown in Fig. 7(a), for a spherical sub-lens, R is the curve radius, p is the sub-aperture of the surface, $n_{\rm c}$ is the refracting index and T is the base thickness of the sub-lens. According to the calculation of NA and thin-lens paraxial approximation:

$$NA = \sin\left(\frac{\varphi_{\rm s}}{2}\right) \approx \frac{p}{2f_{\rm c2}} = \frac{(n_{\rm c} - 1)p}{2R} \tag{12}$$

Therefore:

$$R \approx \frac{(n_{\rm c} - 1)p}{2\sin(\frac{\varphi_{\rm c}}{2})} = \frac{(n_{\rm c} - 1)}{f_{\rm c2}}$$
 (13)

When the sub-beam converging angle φ_s is determined, R is proportional to p and inversely proportional to f_{c2} . As shown in Fig. 7(b), the sub-aperture size p should be constrained due to the predistortion coordinates acquired at the EIP is non-equally spaced, the sub-aperture size p should satisfy:

$$p \le dc_{\min} = \sqrt{(x_{\rm d1} - x_{\rm d4})^2 + (y_{\rm d1} - y_{\rm d4})^2}$$
 (14)

where (x_{d1},y_{d1}) and (x_{d4},y_{d4}) are corresponding to the two arrangement coordinates that have the minimum distance dc_{\min} at the EIP.

In this paper, a sub-lens with the conic surface is used to eliminate the axial spherical aberration. Once p is determined, the initial R and the air space $L_{\rm air}=f_{\rm c2}$ are set according to Eq. (13). The sub-lens is optimized

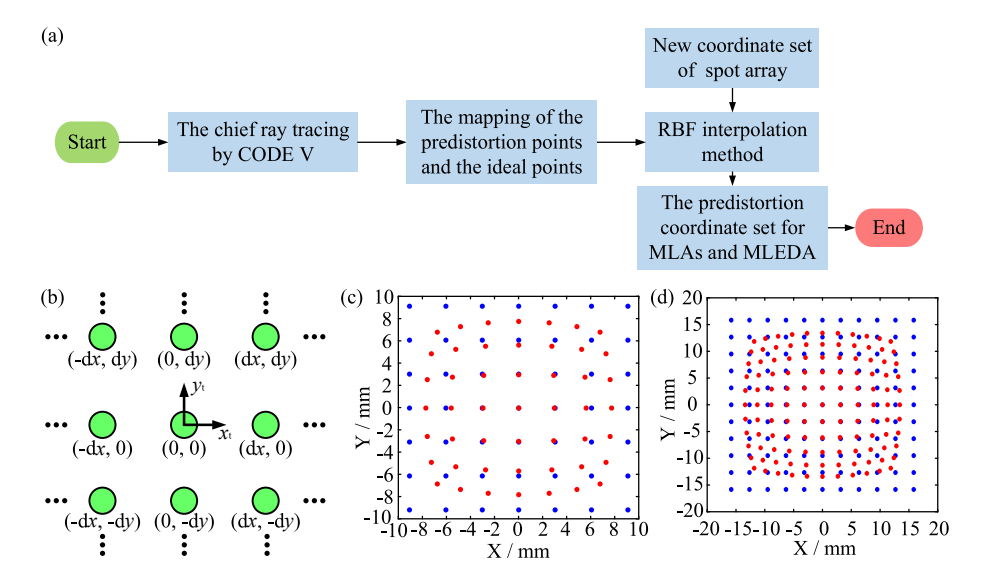


Fig. 6. Predistortion coordinates for eyepieces at EIP. (a) calculation process of the predistortion coordinates; (b) FOVs generation at target plane; chief ray tracing points of (c) 7×7 for eyepiece example 1 and (d) 11×11 points for eyepiece example 2.

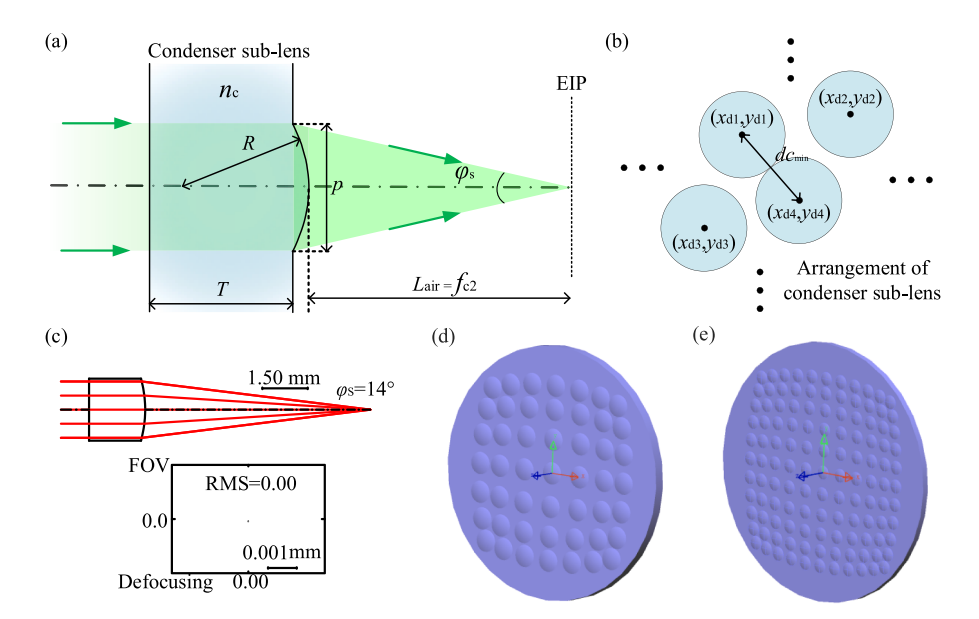


Fig. 7. Surface optimization of sub-lens in condenser MLA. (a) paraxial principle of condenser sub-lens; (b) constraint of the maximum sub-aperture size; (c) optimized sub-lenses with sub-aperture size of 2 mm and $\phi s = 14^{\circ}$; predistortion condenser MLAs correspond to (d) 7×7 sub-lenses for eyepiece example 1 and (e) 11×11 sub-lenses for eyepiece example 2.

to generate the minimum RMS imaging spot and the converging angle is constrained to φ_s at the zero-FOV incident beam. The optimization variables are the curve radius R, the conic parameter K, and the air space $L_{\rm air}$. As shown in Fig. 7(c), a sub-lens example with the material of PMMA can be optimized by CODE V, and the optimized sub-lens can be used for the both two eyepiece examples. The sub-aperture size p is set to 2.0 mm which also satisfies the constraint of Eq. (14). The RMS spot diameter in the sub-lens is optimized to zero because the axial spherical aberration can be reduced by the conic surface. The condenser MLAs with the optimized conic surface corresponding to the two eyepiece examples are shown in Fig. 7(d) and Fig. 7(e). The arrangements of the two MLAs are corresponding to the predistortion coordinates shown in Fig. 6(c) and Fig. 6(d).

3.3. Design of collimating sub-lens for generating collimating sub-beam

The design of collimating MLA includes the arrangement and surface

optimization of the collimating sub-lens. Fortunately, in this paper, the arrangement coordinates of the condenser sub-lens, the collimating sub-lens, and the MLED are identical, therefore, we only need to optimize the surface profile of the collimating sub-lens.

As shown in Fig. 8(a), in the optimization process of the collimating sub-lens, an 580 nm wavelength extended lambert-source MLED with a diameter 0.01 mm and emitting half-angle $\varphi_L=50^\circ$ is used, and the aperture size of collimating sub-lens is 2 mm which equal to the condenser sub-lens. As shown in Fig. 8(b), the optimization process can be divided into two steps:

(1) Collimation optimization by CODE V. The initial structure of the collimating sub-lens can be acquired by the aspheric surface optimization as presented in the design of condenser sub-lens before. As shown in Fig. 8(c), an aspheric sub-lens is optimized at a reverse direction in CODE V, in which the merit function is the RMS spot size. The optimization constraints are like the

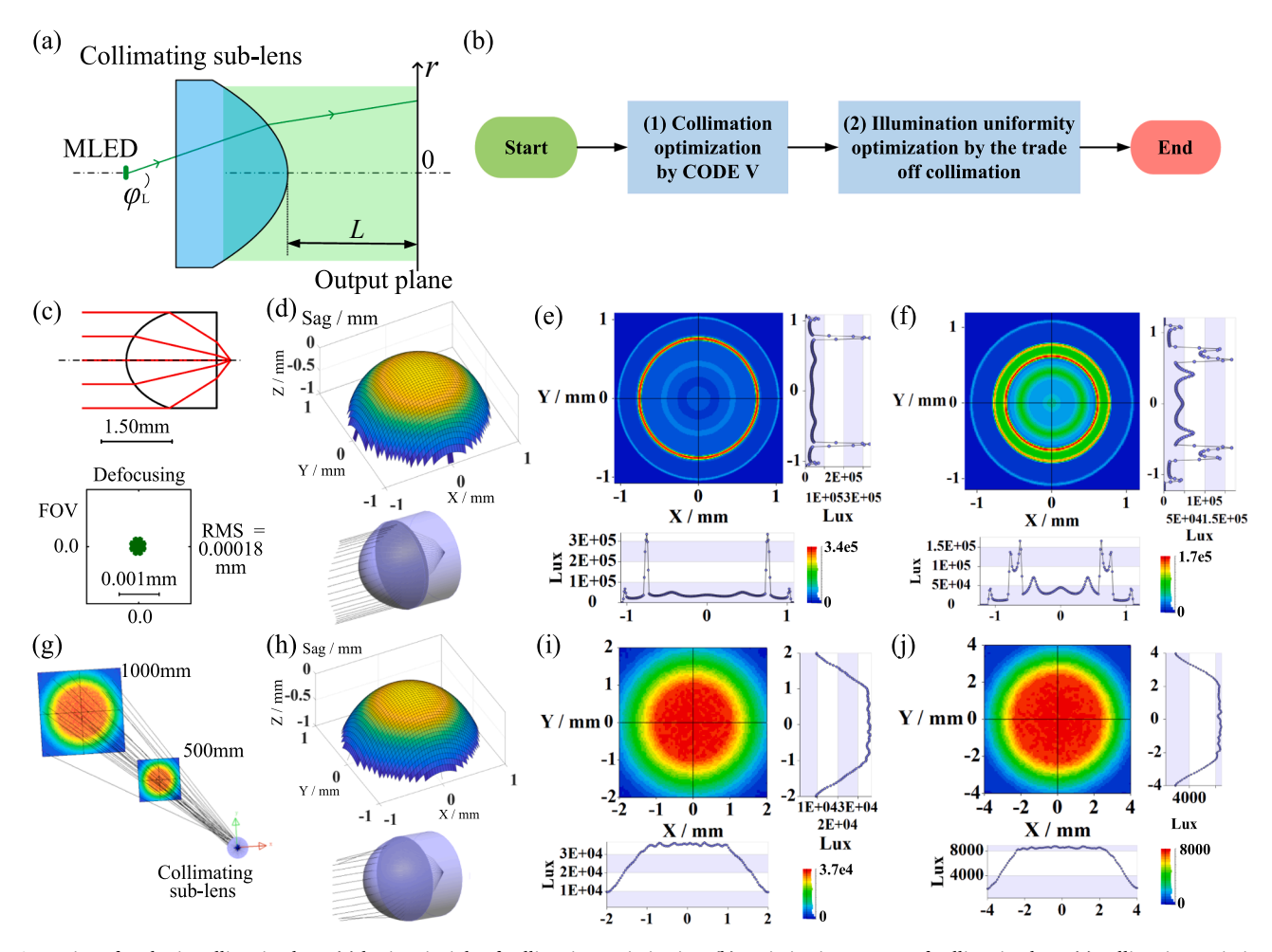


Fig. 8. Design of aspheric collimating lens. (a) basic principle of collimating optimization; (b) optimization process of collimating lens; (c) collimating optimization and analysis; (d) sag analysis after collimating optimization; collimating lens illumination analysis at (e) L = 500 mm and (f) 1000 mm; (g) Monte Carlo ray tracing results after SA optimization; (h) sag analysis of aspheric collimating lens after collimating optimization; illumination analysis in figure (g) at (i) L = 500 mm and (j) 1000 mm.

condenser sub-lens. The RMS spot size is optimized to 0.18 μ m which can be considered as a collimation optimization with a point source. The aspheric surface sag and the 3D structure are given in Fig. 8(d) which shows a smooth aspheric sag acquired after the collimation optimization. As shown in Fig. 8(e) and Fig. 8(f), the illumination analysis is conducted at the target planes of L=500 mm and 1000 mm through the Monte Carlo ray tracing of a 1 lm lambert point source. The illumination distribution is consistently inside the 2 mm aperture range in both near and far fields, demonstrating excellent collimation optimization. However, the optimization only optimizes the ray collimation of the point light source and not consider the energy angle distribution of the light source, so the illumination distributions at the target planes shown in Fig. 8(e) and Fig. 8(f) present great non-uniformity.

(2) Illumination uniformity optimization by the tradeoff collimation. Then, the aspheric sub-lens is optimized to realize collimation and illumination uniformity by the Simulated Annealing (SA) optimization under the extended lambert-source MLED [32–35]. SA is a random searching optimization algorithm which is developed based on the similarity between the annealing process of solid matter and the general combinatorial optimization problem [32]. In this paper, the collimating sub-lens can be optimized by far-field optimization, in which the target plane is set at a far position and the target illumination distribution is set to a uniform distribution. The optimization of the far-field target

can realize the uniformity improvement of illumination distribution in the far field while the collimating optimization can be conducted simultaneously. The merit function (MF) is the relative root-mean-square deviation (RRMSD) between the simulated and target irradiance distributions:

$$RRMSD = \frac{\|\boldsymbol{E}_{t} - \boldsymbol{E}_{s}\|_{F}}{\|\boldsymbol{E}_{t}\|_{F}}$$
 (15)

where E_t and E_s denote the matrices of the target and simulated illumination distributions respectively, and $||\cdot||_F$ is the Frobenius norm. In this paper, LightTools is used for illumination analysis based on Monte-Carlo ray tracing. MATLAB can read the data of the simulated illumination distribution and calculate the MF value.

An optimization example is given here: in the optimization, the output plane is set at 1000 mm (the merit function is corresponding to the target zone within the radius of 3 mm) from the MLED. The optimization constraints are the light efficiency which constrains the light loss and the conic parameters of the aspheric sub-lens which affect the surface shape. The optimization results are shown in Fig. 8(g). The sag of the aspheric surface and the 3D structure are given in Fig. 8(h) which shows a smooth aspheric surface acquired after the optimization. The illumination analysis of the target planes at L=500 mm and 1000 mm through the Monte Carlo ray tracing are shown in Fig. 8(i) and Fig. 8(j). In this optimization, illumination uniformity is emphasized and the collimation of the beam is relatively sacrificed, the overall distribution of illumination is always beyond the 2 mm aperture range in the near

(500 mm) and far (1000 mm) fields. In addition, the light efficiency of the optimized sub-lens is nearly 32%. However, the flattop illumination distribution is realized which reflect the illumination uniformity has been improved unprecedentedly in the near (500 mm) and far (1000 mm) fields. In addition, for the same sub-source MLED, the same collimating sub-lens can be used. In this paper, the two design examples are assumed to use the same MLED, therefore, only the arrangement coordinates of the sub-lens or MLED are different. With the rapid development of current MLED preparation technology and application technology[41], a large number of MLED with special application significance has been designed and implemented [42,43]. The light source utilized in the proposed system is not limited to the MLED. In fact, the smaller light source are preferred for optimal performance; diameters less than 0.01 mm yield superior results. Additionally, since the light source array must achieve the predistortion spatial arrangement, it also needs the LED array arrangement technology with high precision, which is mature at present.

4. Simulations and analysis

In this section, to verify the two kinds of spot array projection systems proposed in this paper, we will conduct an overall non-sequential ray tracing and illumination analysis on the total system consisting of the projection eyepiece and two kinds of MLAs designed and implemented in section 3. The effects and applications for the near field and far field are analyzed and discussed in section 4.1 and section 4.2 separately. The predefined-geometry arrangement spot array is analyzed in section 4.3.

4.1. Near-field spot-array projection

In the near field spot array projection simulations, the light source is

MLEDA which consists of some 1 lm equal-power MLEDs with a diameter size of 0.01 mm. As shown in Fig. 9(a), a near-field $L_p = 200$ mm Monte-Carlo ray tracing is conducted for the spot-array projector example 1 which realized a diagonal projection FOV of 80°. The EPD size is set to 4 mm which is also the maximum EPD size of the spot-array projector example 1. The receiver resolution at the target plane is set to 2000 \times 2000. The EIP plane shows the barrel predistortion spot array with a uniform illumination distribution and the spot array projected at the target plane shows a regular equal-spaced spot array distribution. The overall and local illumination results at $L_p = 100$ mm, 200 mm, and 300 mm near filed target planes are shown in Fig. 9(b), Fig. 9(c), and Fig. 9(d) correspondingly. In the near-field area, due to the relatively close projection distance, the overall illumination distribution of the projected spot array is mainly affected by the aberration introduced by the eyepiece. As shown in Fig. 9(b), the distribution of local illumination increases (inside the red dashed box) due to certain deformation of the spot in the edge FOV, but the overall relative illumination is higher than 82%. Since each sub-beam has a certain divergence angle due to the imperfect designs of the eyepiece and collimating sub-lens, when the optical path of the sub-beam corresponding to the edge FOV gradually increases, the edge FOV projection spot size increases faster than the central-FOV spot. Due to the use of equal-power sub-source, the spot illumination of the edge FOV will gradually decrease faster than the central FOV with the increase of the projection distance. As shown in Fig. 9(c), the spot array projection achieves the best effect at $L_p = 200$ mm, both the local spot illumination distribution and the overall relative illumination are higher than 90%. As shown in Fig. 9(d), the relative illumination of the edge-FOV spot at $L_p = 300$ mm is lower than the center-FOV spot, but the overall relative illumination is higher than 80%. Due to the pre-distortion arrangement of MLA and MLED, the large-angle array spot projection is corrected, and the maximum distortion of the projected spot array is less than 0.5% at the three near-

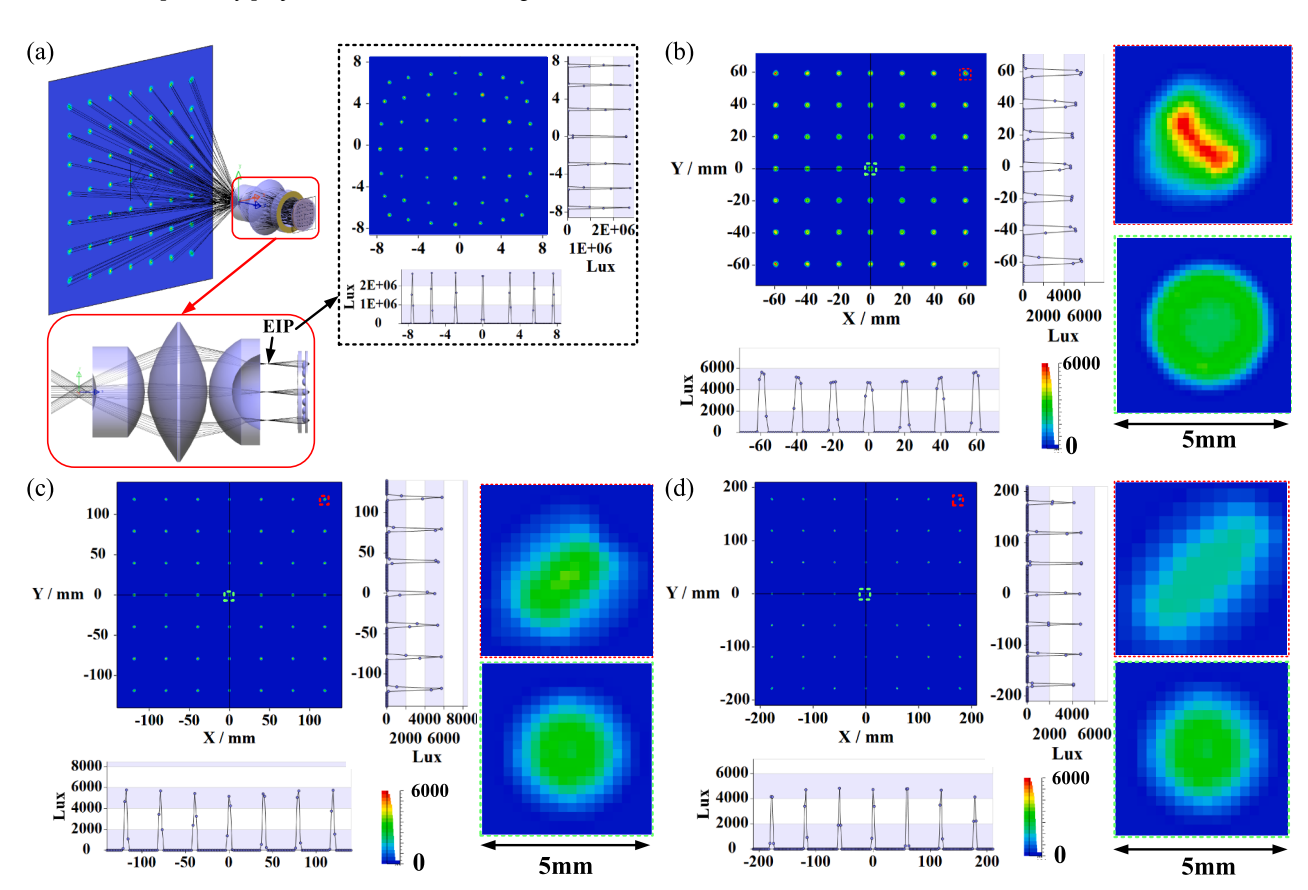


Fig. 9. Near field simulations of spot-array projector example 1. (a) near-field Monte-Carlo ray tracing; overall and local illumination results at (b) $L_p = 100$ mm, (c) 200 mm and (d) 300 mm near filed target planes correspondingly.

fields distances (the geometry center coordinates of near-field spot are used as the evaluation quantity, and the result may be lower than expected due to the slight deformation of edge-FOV spot). Furthermore, as shown in Fig. 9, a good stray-light suppression in the near field can be realized by the spot array projector example 1(There is no stray light energy on the target plane except the projected spot array).

As shown in Fig. 10(a), a near-field $L_p = 200$ mm Monte-Carlo ray tracing is conducted for the spot-array projector example 2 which realized a diagonal projection FOV of 100° . The EPD size is set to 4.5 mm which is also the maximum EPD size of the spot-array projector example 2. The receiver resolution at the target plane is set to 2000 \times 2000. The EIP plane shows the barrel predistortion spot array with a uniform illumination distribution and the spot array projection at the target plane shows a regular equal-spaced spot array. The overall and local illumination results at $L_p = 100$ mm, 200 mm, and 300 mm near filed target planes are shown in Fig. 10(b), Fig. 10(c), and Fig. 10(d) correspondingly. As shown in Fig. 10(b), the spot distribution of local illumination increases (inside the red dashed box) due to certain deformation of the spot in the edge FOV, but the overall relative illumination is higher than 74%. As shown in Fig. 10(c), the spot array projection achieves the best effect at $L_p = 200$ mm, and the overall relative illumination is higher than 85%. As shown in Fig. 10(d), the relative illumination of the edge-FOV spot at $L_{\rm p}=300$ mm is lower than the center-FOV spot, but the overall relative illumination is still higher than 80%. In addition to the causes of uneven distribution and variation of illumination analyzed before, the irregular features of the local projected spots at the edge FOVs are also influenced by the sawtooth microstructure of the Fresnel lens. The maximum distortion of the projected spot array is less than 0.9% at the three near-fields distances. Furthermore, as shown in Fig. 10, a good stray-light suppression in the near field can be realized by the spot array projector example 2.

In the near-field projection of the proposed spot array projector, the size or the geometry of the projection spot can be changed by adjusting the size or the opening shape of the diaphragm EPD. As shown in Fig. 11, the near-field adjustable spot projection is simulated. The simulations of near-field spot array projection in example 1 are shown in Fig. 11(a) and Fig. 11(b) which correspond to the EPD size of 3 mm and 1 mm (the projection distance is set to 100 mm). Comparing the maximum size of EPD (4 mm in Fig. 9), the results show that the spot size is smaller when the EPD is reduced. However, since the size of the spot is adjusted by energy apodization, as the opening size of the EPD decreases, the spot energy on the projection surface starts to decrease in proportion to the reduction in the area of the aperture. The simulations of near-field predefined spot array projection in example 1 are shown in Fig. 11(c) and Fig. 11(d) which correspond to the EPD opening geometry of a fivepointed star and annulus (the projection distance is set to 100 mm, the opening size of EPD is kept as the maximum). The illumination uniformity of each projected spot and the overall spot array is the same as that of the system under the initial circular aperture as simulated in Fig. 9. In addition, the simulations of near-field spot array projection in example 2 are shown in Fig. 11(e) and Fig. 11(f) which corresponds to the EPD size of 3 mm and 1 mm (the projection distance is set to 100 mm). The characteristics and factors of illumination attenuation for the projected spot are the same as those illustrated in example 1 above. The simulations of near-field pre-defined spot array projection in example 2 are shown in Fig. 11(g) and Fig. 11(h) which correspond to the EPD

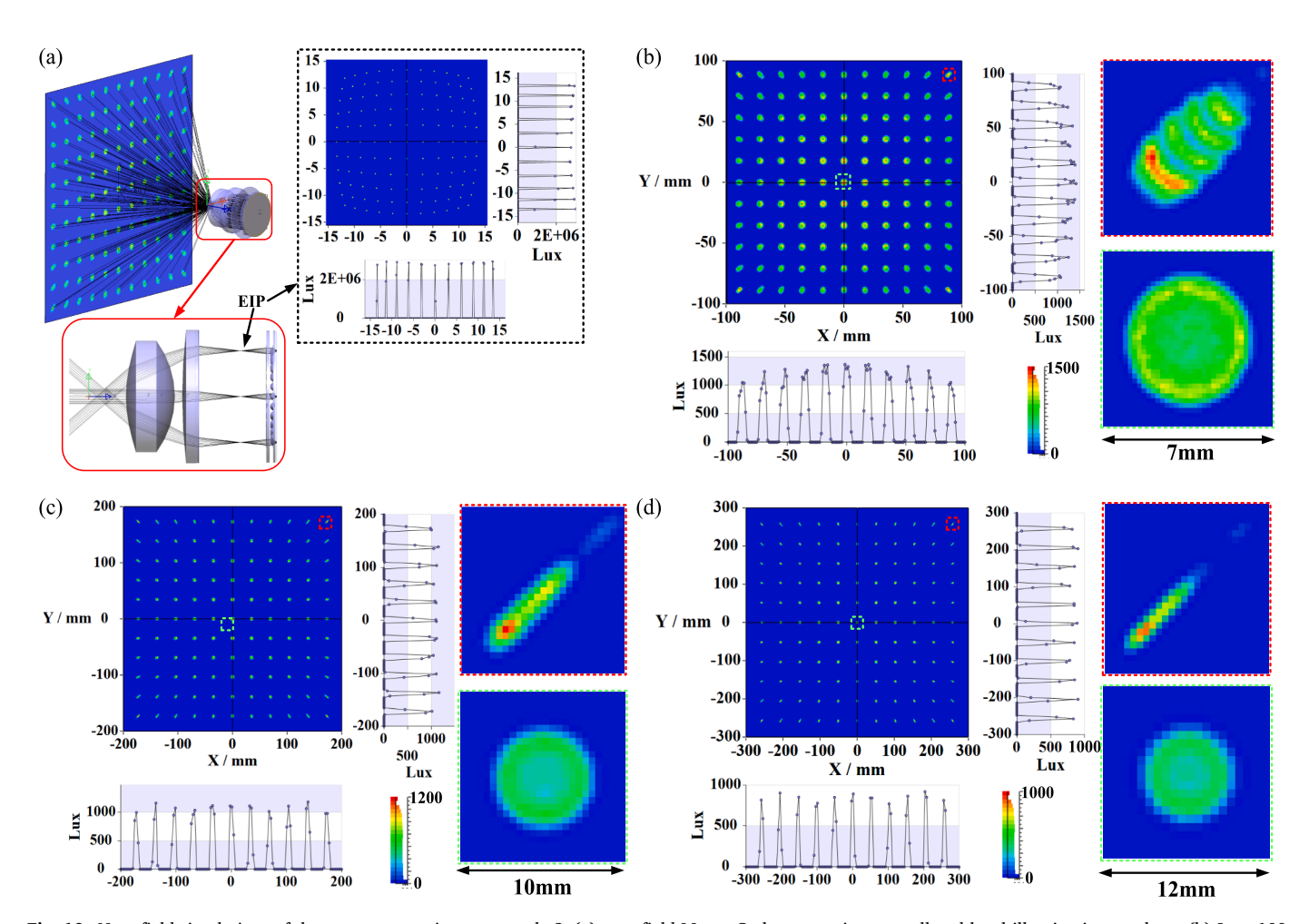


Fig. 10. Near field simulations of the spot-array projector example 2. (a) near-field Monte-Carlo ray tracing; overall and local illumination results at (b) $L_p = 100$ mm, (c) 200 mm and (d) 300 mm near filed target planes correspondingly.

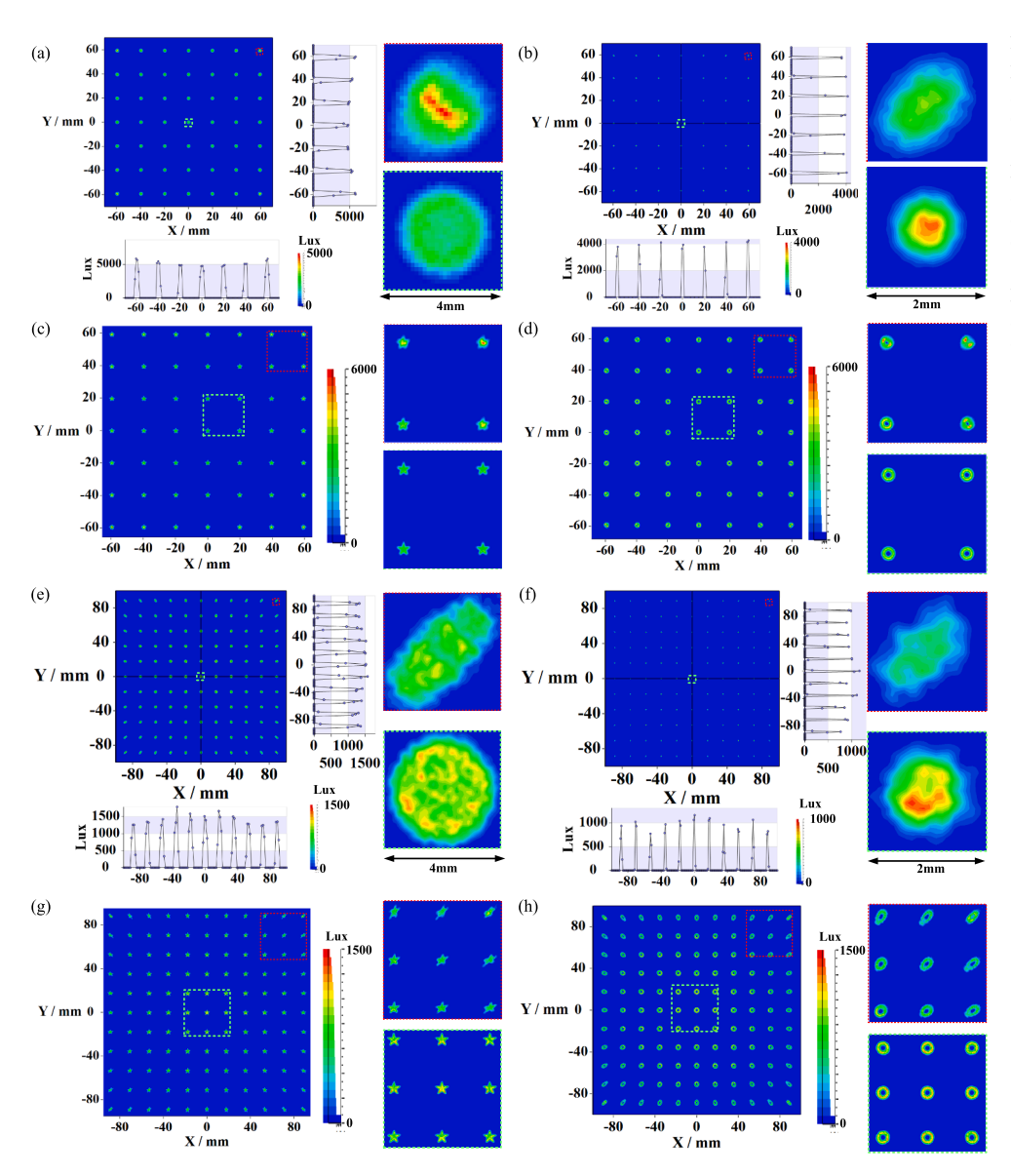


Fig. 11. Simulations of near-field spot array projection with different spot sizes and spot geometry. Near-field spot array projection in example 1 with EPD size of (a) 3 mm and (b) 1 mm. Simulations of near-field spot array projection in example 1 with EPD opening geometry of (c) five-pointed star and (d) annulus. Near-field spot array projection in example 2 with EPD size of (e) 3 mm and (f) 1 mm. Simulations of near-field spot array projection in example 2 with EPD opening geometry of (g) five-pointed star and (h) annulus

opening geometry of a five-pointed star and annulus (the projection distance is set to 100 mm, the opening size of EPD is kept as the maximum). Furthermore, the pre-defined geometric pattern light spot corresponding to the edge FOV is distorted due to the large-FOV spot projection aberration and Fresnel surface shape.

4.2. Far-field spot-array projection

We also analyzed and simulated the far-field spot array projection of the two design examples. In the following far-field analysis, compared with the near-field spot projection, the projection distance is different, and the power of MLED light source at different spatial locations is also different. As shown in Fig. 12(a), a far-field (1000 mm, 3000 mm, and 5000 mm) Monte-Carlo ray tracing is conducted for the spot-array projector example 1 which realized a diagonal projection FOV of 80°. As discussed above, when the projection distance gradually increases, the illumination of the edge-FOV spot gradually decreases. In the far-field projection, the illumination of the edge-FOV spot decreases sharply, so it is necessary to adjust the power distribution of the MLED source to compensate for the low contrast phenomenon at the edge FOV. The power matching of MLEDA is used to achieve far-field uniformity: by adjusting the power distribution of MLED at different spatial

positions, the illumination distribution of light spots at different spatial positions on the target surface is more consistent. Here, a simple illumination compensation method is conducted based on the initial curve analysis of the relative illumination distribution of the eyepiece as shown in Fig. 4(h). The power distribution of MLEDA is given by quadratic polynomial fitting. Through the iterative optimization of quadratic polynomial parameters, the illumination distribution of 3000 mm far-field spot array can reach the most uniform. When the quadratic polynomial of MLEDA power is obtained, the MLED power in different radial positions is allocated by interpolation. (both the illumination distribution at the target surface and the power distribution of the MLEDA meet the axial symmetry). Furthermore, as shown in Fig. 12, a good stray-light suppression in the far field can be realized by the spot array projector example 1.

As shown in Fig. 12(a), the illumination distribution at the EIP plane not only presents the space arrangement positions but also the power distribution of the MLEDA. The overall and local illumination results at $L_{\rm p}=1000$ mm, 3000 mm and 5000 mm far-filed target planes are shown in Fig. 12(b), Fig. 12(c), and Fig. 12(d) correspondingly. In this paper, we considered the far-filed illumination compensation at the projection distance of 3000 mm, therefore, the illumination uniformity of the spot array would decrease at other distances. As shown in Fig. 12(c), the best

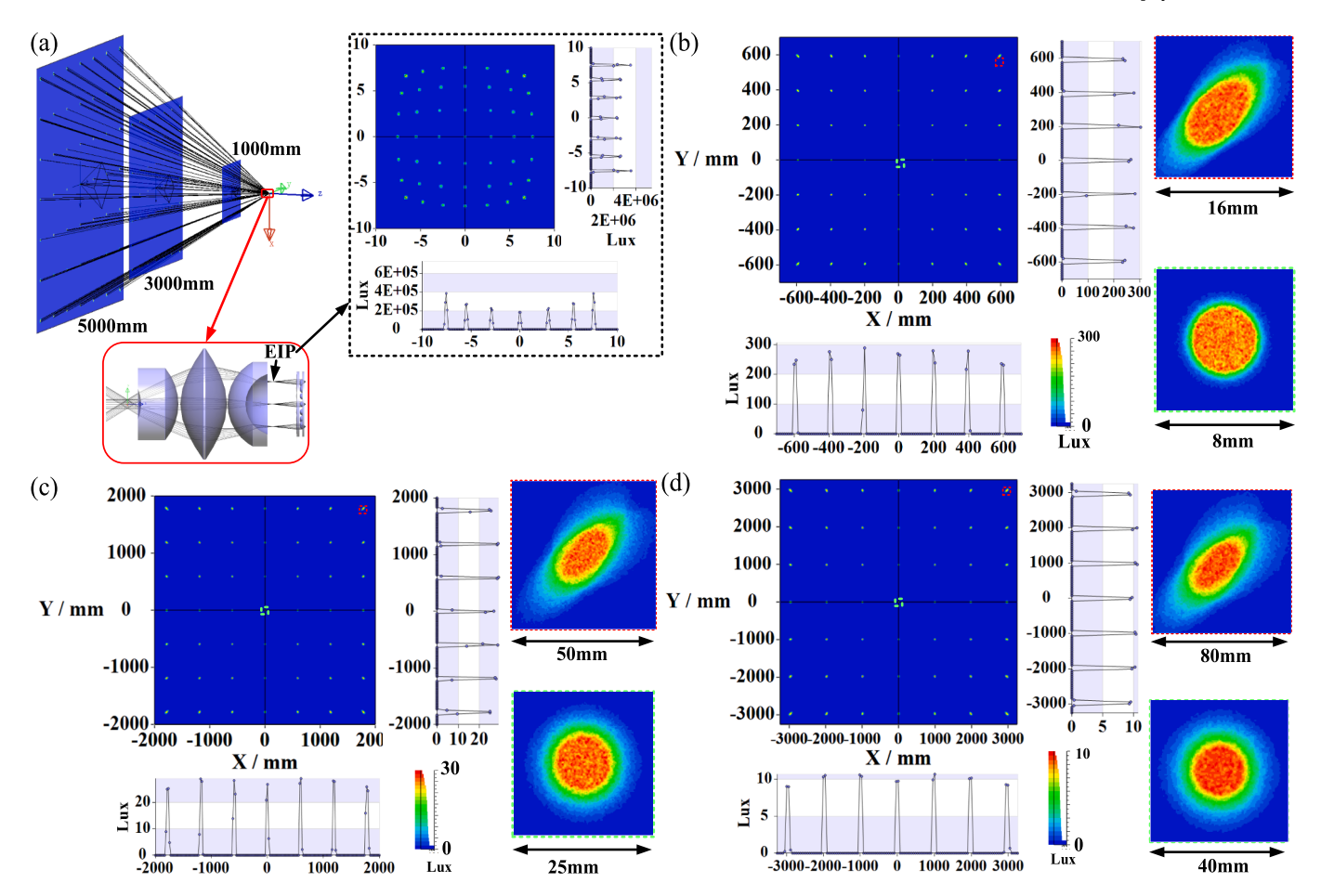


Fig. 12. Near field simulations of the spot-array projector example 1. (a) near-field Monte-Carlo ray tracing; overall and local illumination results at (b) $L_p = 1000$ mm, (c) 3000 mm and (d) 5000 mm near filed target planes correspondingly.

relative illumination effect nearly 81% is achieved in 3000 mm. The spot array projection of the overall relative illumination is higher than 70% which meets the common far-field application requirements. The maximum distortion of the projected spot is less than 0.1% at the three far-fields distances (the far-field distortion correction can hardly be influenced due to the slight deformation of edge-FOV spot).

As shown in Fig. 13(a), a far-field (1000 mm, 3000 mm, and 5000 mm) Monte-Carlo ray tracing is conducted for the spot-array projector example 2 which realized a diagonal projection FOV of 100° . The overall and local illumination results at $L_p=1000~\text{mm}$, 3000 mm and 5000 mm far-filed target planes are shown in Fig. 13(b), Fig. 13(c), and Fig. 13(d) correspondingly. By increasing the MLED power of the edge FOV, we can balance the spot illumination of the full FOV. Although the distribution of illumination is high at the edge FOV and low at the center FOV when the projection is 1000 mm, the distribution of illumination is changed to be uniform as the projection distance increases, as shown in Fig. 13(c), and Fig. 13(d). The spot array projection of the overall relative illumination is nearly 80% in 3000 mm. Since the projection of the far-field spot array generally only cares about whether the energy is sufficient, we no longer carry out the analysis of far-field spot size and geometry. The two design examples in the above far-field analysis work under their maximum EPD size correspondingly. The maximum distortion of the projected spot is less than 0.3% at the three far-fields distances. Furthermore, as shown in Fig. 13, a good stray-light suppression in the far field can be realized by the spot array projector example 2.

4.3. Pattern spot-array projection

The projection distribution of spot arrays with different patterns can

also be realized by the position arrangement of sub-lens and MLED. As shown in Fig. 14, a 'smile' pattern spot projection is realized by the spotarray projector example 1. The predefined illumination distribution is shown in Fig. 14(a), and the blue asterisk marks are labeled which presents the coordinates of the spots. The predistortion coordinates at the EIP plane as well as the arrangement positions of the sub-lens are shown in Fig. 14(b), in which the coordinates are acquired by the RBF interpolation method detailed before. The generated condenser MLA is shown in Fig. 14(c). The Monte Carlo ray-tracing and illumination simulation results of near-field (200 mm) spot array projection are shown in Fig. 14(d), and the Monte Carlo ray-tracing and illumination simulation results of far-field (3000 mm) spot array projection are shown in Fig. 14(e). A sharp and no stray light 'smile' pattern spot array projection is realized.

As shown in Fig. 15, an 'XJTU' pattern spot projection is realized by the spot-array projector example 2. The predefined illumination distribution is shown in Fig. 15(a), and the blue asterisk marks are labeled which presents the coordinates of the spots. The predistortion coordinates at the EIP plane as well as the arrangement positions of the sub-lens are shown in Fig. 15(b), in which the coordinates are acquired by the RBF interpolation method detailed before. The generated condenser MLA is shown in Fig. 15(c). The ray-tracing and illumination simulation results of near-field (200 mm) spot array projection are shown in Fig. 15(d), and the ray-tracing and illumination simulation results of far-field (3000 mm) spot array projection are shown in Fig. 15 (e). A sharp and no stray light 'XJTU' pattern spot array projection is realized. The parameters of sources and the surface profiles in each eyepiece and sub-lens of MLAs are the same as used in section 4.1 and section 4.2.

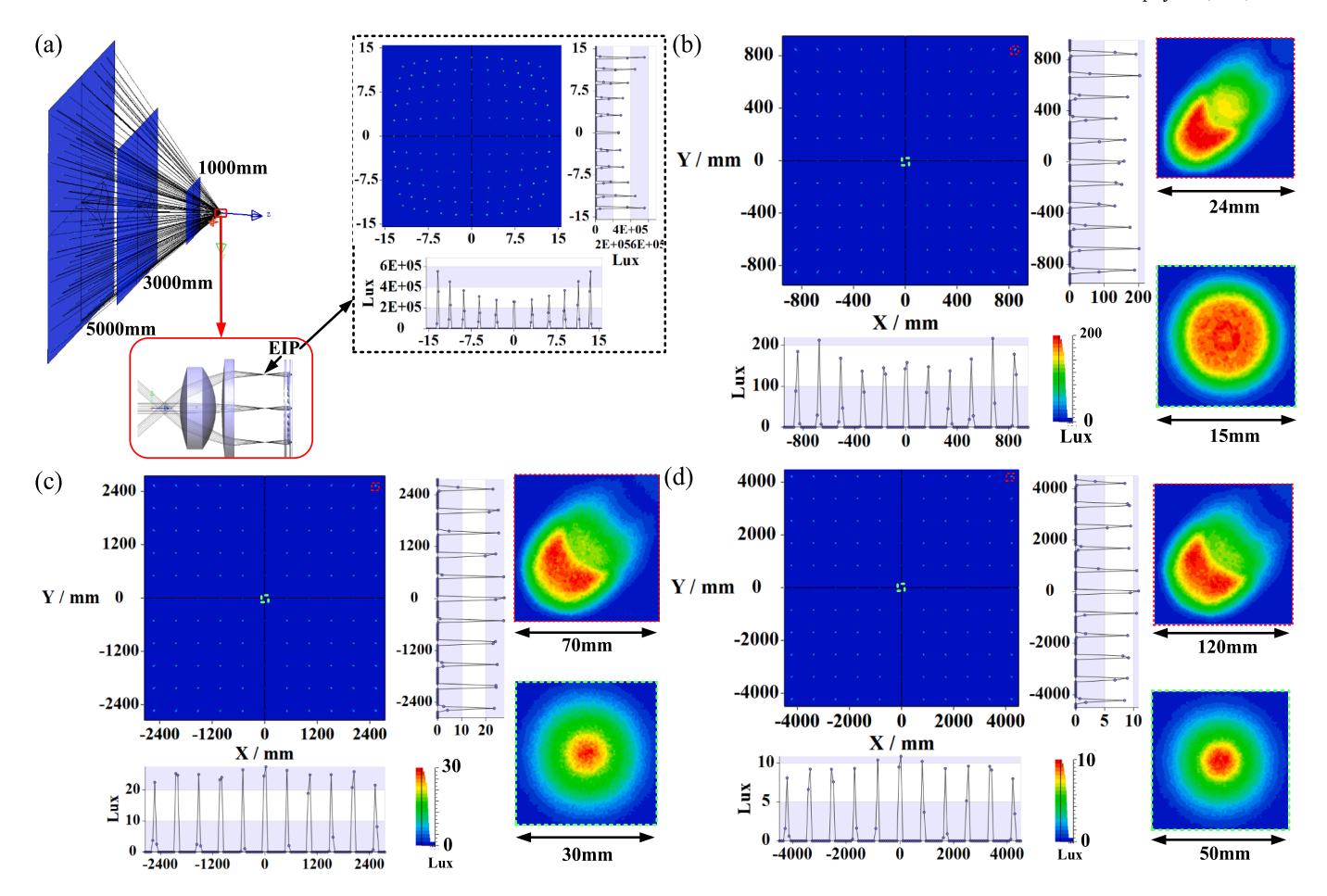


Fig. 13. Near field simulations of the spot-array projector example 1. (a) near-field Monte-Carlo ray tracing; overall and local illumination results at (b) $L_p = 1000$ mm, (c) 3000 mm and (d) 5000 mm near filed target planes correspondingly.

5. Conclusion and prospect

This paper proposed a design method for a large-angle, distortion-free and spot adjustable LED spot array projector composed of two MLAs and an eyepiece. By optimizing the eyepiece imaging system, collimating MLA, and condenser MLA, a large-angle LED spot array projector can be obtained. The eyepiece system is optimized using an imaging optical optimization method to project the sub-beams at a large angle to the target plane. The collimating MLA is optimized using a SA method to achieve collimation and far-field homogenization of the MLEDA. The condenser MLA is also optimized using an imaging optical optimization method to achieve the refocusing of the collimating beam and the matching of the NA with the eyepiece. Moreover, the RBF interpolation method is employed to predefine the arrangements of the MLEDA and the sub-lens on the two MLAs, which can correct the large-angle distortion introduced by the eyepiece.

In addition, the spot-array projector's near-field and far-field application situations are considered and analyzed. In the near-field situation, adjustable opening geometry (size and shape) of the eyepiece diaphragm can be used to achieve different spot geometry at the near-filed target plane. In the far-field situation, the power matching of MLEDA is used to realize a far-filed uniformity of spot array. The predefined-geometry arrangement spot array projector is also proposed and verified in the near and far field. Design examples based on two types of eyepieces are given and analyzed to validate the method we proposed. The first example is based on the eyepiece structure of the classic Zeiss Astroplan eyepiece, which realized a full-FOV projection of 80°. The second example is based on a Fresnel lens with a planar base which realized a full-FOV projection of 100°. Comparing to the DOE and

freeform-based spot array generators, the proposed spot array projector only uses spheric and aspheric surfaces, which are currently mature in application and production, resulting in higher stability and lower process sensitivity, and it also has the advantages such as: without central-FOV peak spot, more uniform, free of large-angle distortion and stray-light suppression.

This paper primarily focuses on the design method and analysis of the proposed LED spot array projector system. However, there are still some areas that require further attention in future research, such as addressing the distortion and non-uniform distribution issues of the large-FOV projected spot, as well as addressing the illumination decrease problem in large far-field projections (although this has been addressed to some extent by compensating for the MLED with different source power in this paper). Additionally, we plan to further advance the research on spot array projection by exploring methods to improve light efficiency, and conducting specific experimental verifications.

CRediT authorship contribution statement

Yue Liu: Writing – review & editing. Jingping Zhu: Writing – review & editing. Chen Chen: Writing – review & editing. Xun Hou: Writing – review & editing.

Declaration of Competing Interest

The authors declare that they have no known competing financial interests or personal relationships that could have appeared to influence the work reported in this paper.

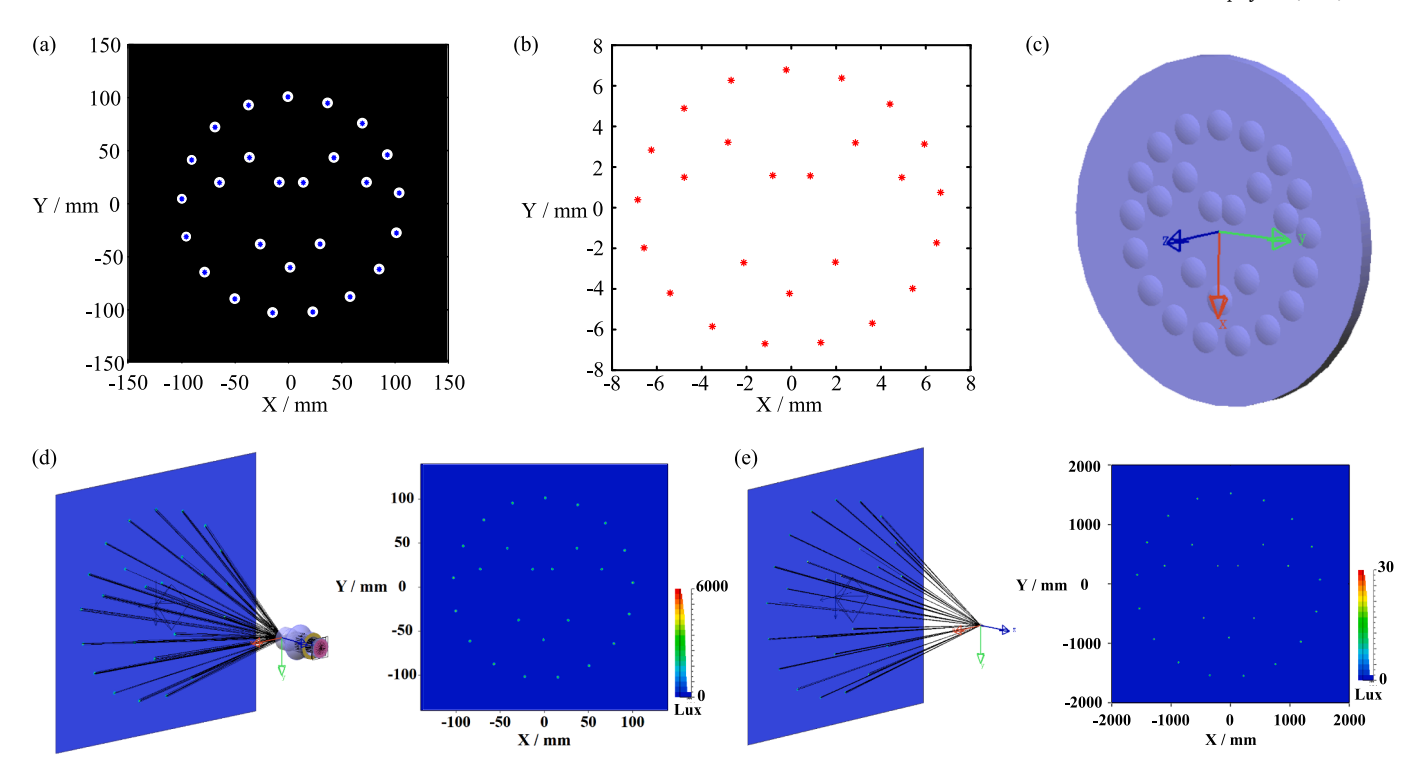


Fig. 14. Smile pattern spot projection realized by the spot-array projector example 1. (a) predefined illumination distribution of smile pattern spot projection; (b) predistortion coordinates at the EIP plane as well as the arrangement positions of the sub-lens and MLED; (c) generated condenser MLA; ray-tracing and illumination simulation results of (d) near-field (200 mm) and (e) far-field (3000 mm) spot array projection.

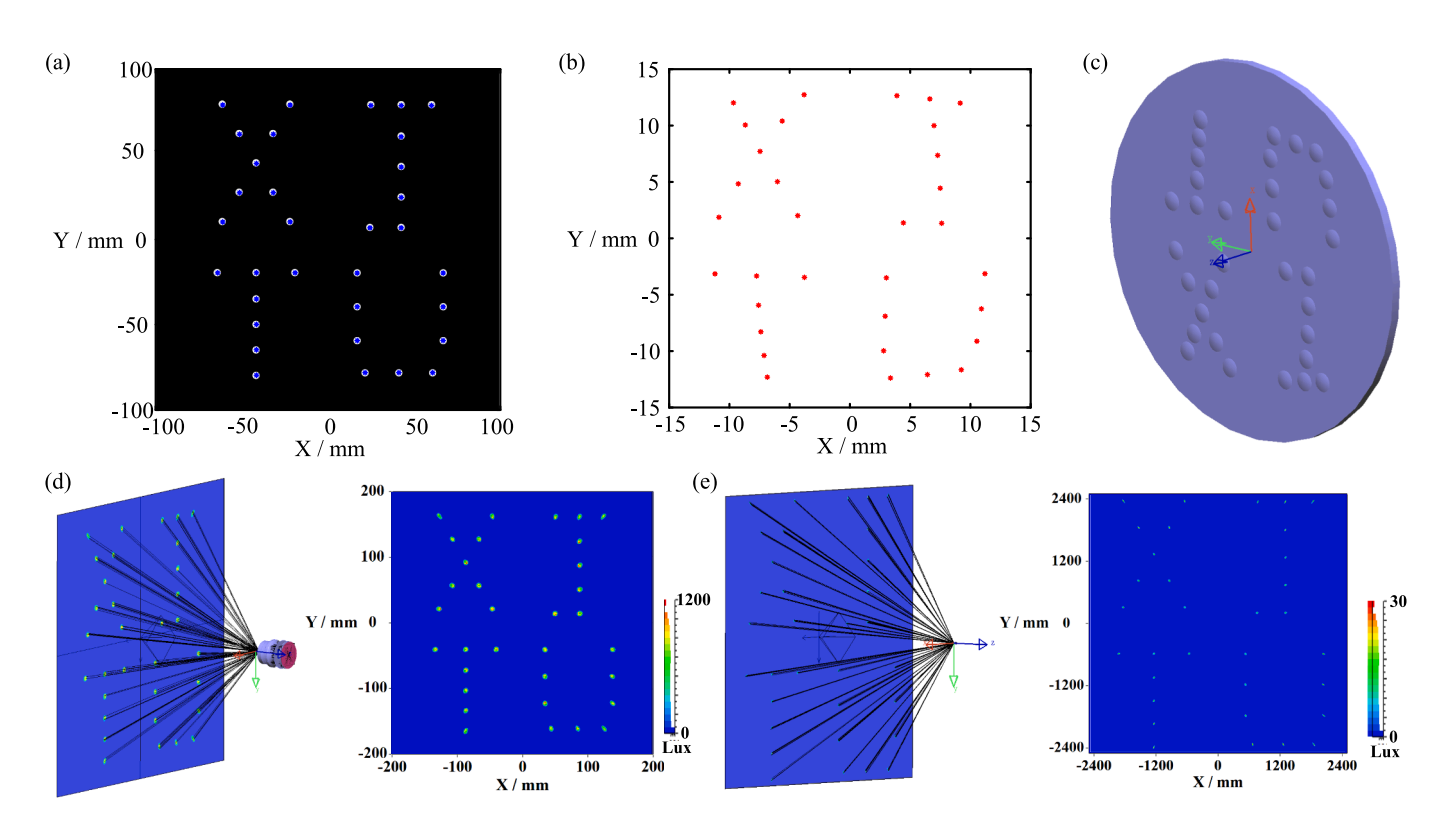


Fig. 15. 'XJTU' pattern spot projection realized by the spot-array projector example 2. (a) predefined illumination distribution of 'XJTU' pattern spot projection; (b) predistortion coordinates at the EIP plane as well as the arrangement positions of the sub-lens and MLED; (c) generated condenser MLA; ray-tracing and illumination simulation results of (d) near-field (200 mm) and (e) far-field (3000 mm) spot array projection.

Data availability

Data underlying the results presented in this paper are not publicly available at this time but may be obtained from the authors upon reasonable request.

Acknowledgments

This work is funded by National Natural Science Foundation of China (Grant No. 61890961, 62127813); Natural Science Basic Research Plan in Shaanxi Province of China (Program No. 2018JM6008). We would like to thank Synopsys and Shang Hai OE Technology Co, LTD for providing the technical support of CODE V and LightTools.

References

- [1] H. Kim, J.K. Hwang, M. Jung, J. Choi, H.W. Kang, Laser-induced optical breakdown effects of micro-lens arrays and diffractive optical elements on ex vivo porcine skin after 1064 nm picosecond laser irradiation, Biomed. Opt. Express 11 (12) (2020) 7286–7298.
- [2] W. Ge, C. Xing, V. Veiko, Z. Li, All-optical, self-focused laser beam array for parallel laser surface processing, Opt. Express 27 (20) (2019) 29261–29272.
- [3] E.V. Adamov, V.P. Aksenov, V.V. Atuchin, V.V. Dudorov, V.V. Kolosov, M. E. Levitsky, Laser beam shaping based on amplitude-phase control of fiber laser array, OSA Continuum 4 (1) (2021) 182–192.
- [4] M.A. Golub, Laser Beam Splitting by Diffractive Optics, Opt. Photonics News 15 (2) (2004) 36–41.
- [5] M. Jarczynski, T. Mitra, M. Ivanenko, L. Aschke, C. Wächter, U. Fuchs, T. Linke, S. Kiontke, Monolithic optical components for splitting of high-power beams, Proc. SPIE 8490 (2012) 849000.
- [6] M. Maksimovic, Design and optimization of compact freeform lens array for laser beam splitting: A case study in optimal surface representation, Proc. SPIE 9131 (2014), 913107.
- [7] J. Si, Z. Feng, D. Cheng, Y. Wang, Freeform beam splitting system design for generating an array of identical sub-beams, Opt. Express 29 (19) (2021) 29918.
- [8] F.M. Dickey, S.C. Holswade, D.L. Shealy, eds. Laser beam shaping applications, CRC, (2006) 149–152.
- [9] B. Qin, X. Li, Z. Yao, J. Huang, Y. Liu, A. Wang, S. Gao, S. Zhou, Z. Wang, Fabrication of microlenses with continuously variable numerical aperture through a temporally shaped femtosecond laser, Opt. Express 29 (3) (2021) 4596–4606.
- [10] S. Wang, L. Kong, C. Wang, C. Cheung, Ultra-precision manufacturing of microlens arrays using an optimum machining process chain, Opt. Express 31 (2) (2023) 2234
- [11] G. Yan, Y. Zhang, K. You, Z. Li, Y. Yuan, F. Fang, Off-spindle-axis spiral grinding of aspheric microlens array mold inserts, Opt. Express 27 (8) (2019) 10873–10889.
- [12] T. Aderneuer, O. Fernandez, A. Karpik, J. Werder, M. Marhöfer, P. Magnus Kristiansen, R. Ferrini, Surface topology and functionality of freeform microlens arrays, Opt. Express 29 (4) (2021) 5033.
- [13] F. Fang, N. Zhang, X. Zhang, Precision injection molding of freeform optics, Adv. Opt. Technol. 5 (4) (2016) 303–324.
- [14] W.X. Zhao, H.L. Zhang, Q.L. Ji, H. Deng, D.H. Li, Dual-side see-through integral imaging 3D display system based on lens array holographic optical element, Displays 70 (2021), 102093.
- [15] S.L. Pang, T.H. Wang, F.Y. Zhong, L.B. Zhang, H. Deng, Y. Xing, Tabletop integral imaging 3D display system based on annular point light source, Displays 69 (2021), 102029.
- [16] Z. Qin, Y. Zhang, B.-R. Yang, Interaction between sampled rays' defocusing and number on accommodative response in integral imaging near-eye light field displays, Opt. Express 29 (5) (2021) 7342.

- [17] Q. Yang, Design study of a compact ultra-wide-angle high-spatial-resolution high-spectral-resolution snapshot imaging spectrometer, Opt. Express 29 (2) (2021) 2893
- [18] N.S. Holliman, N.A. Dodgson, G.E. Favalora, L. Pockett, Three-Dimensional Displays: A Review and Applications Analysis, IEEE Trans. Broadcast 57 (2) (2011) 362–371.
- [19] Y. Liu, D. Cheng, T. Yang, Y. Wang, High precision integrated projection imaging optical design based on MLA", Opt. Express 27 (9) (2019) 12264–12281.
- [20] M. Prossotowicz, D. Flamm, A. Heimes, F. Jansen, H.-J. Otto, A. Budnicki, A. Killi, U. Morgner, Dynamic focus shaping with mixed-aperture coherent beam combining, Opt. Lett. 46 (7) (2021) 1660.
- [21] M. Zimmermann, N.R.V. Lindlein, K.J. Weible, Microlens laser beam homogenizer—from theory to application, Proc. SPIE 6663 (2007), 666302.
- [22] T. Kim, S. Hwang, D. Park, T.J. Yu, Performance of zoom homogenizer to control the size of illumination field, Appl. Opt. 58 (9) (2019) 2429–2437.
- [23] Y. Jin, A. Hassan, Y. Jiang, Freeform MLA homogenizer for excimer laser beam shaping, Opt. Express 24 (22) (2016) 24846–24858.
- [24] Y. Liu, D. Cheng, Q. Hou, H. Chen, Z. Feng, T. Yang, Y. Wang, Compact integrator design for short-distance sharp and unconventional geometric irradiance tailoring, Appl. Opt. 60 (14) (2021) 4165.
- [25] K. Desnijder, W. Ryckaert, P. Hanselaer, Y. Meuret, Luminance spreading freeform lens arrays with accurate intensity control, Opt. Express 27 (23) (2019) 32994–33004.
- [26] S. Zhao, K. Wang, F. Chen, Z. Qin, S. Liu, Integral freeform illumination lens design of LED based pico-projector, Appl. Opt. 52 (13) (2013) 2985–2993.
- [27] D. Cheng, Q. Wang, Y. Liu, H. Chen, D. Ni, X. Wang, C. Yao, Q. Hou, W. Hou, G. Luo, Y. Wang, Design and manufacture AR head-mounted displays: A review and outlook, Light: Adv. Manuf. 2 (2021) 24.
- [28] C.P. Chen, L. Zhou, J. Ge, Y. Wu, L. Mi, Y. Wu, B. Yu, Y. Li, Design of retinal projection displays enabling vision correction, Opt. Express 25 (23) (2017) 28223–28235.
- [29] J. Chen, L. Mi, C.P. Chen, H. Liu, J. Jiang, W. Zhang, Design of foveated contact lens display for augmented reality, Opt. Express 27 (26) (2019) 38204–38219.
- [30] M.Y. He, D. Wang, Y. Xing, Y.W. Zheng, H.L. Zhang, X.L. Ma, R.Y. Yuan, Q. H. Wang, Compact and lightweight optical see-through holographic near-eye display based on holographic lens, Displays 70 (2021), 102104.
- [31] C.P. Chen, L. Mi, W. Zhang, J. Ye, G. Li, Waveguide-based near-eye display with dual-channel exit pupil expander, Displays 67 (2021), 101998.
- [32] S. Kirkpatrick, C.D. Gelatt, M.P. Vecchi, Optimization by Simulated Annealing, Science 220 (4598) (1983) 671–680.
- [33] R.J. Koshel, Simplex optimization method for illumination design, Opt. Lett. 30 (6) (2005) 649–651.
- [34] R.J. Koshel, Aspects of illumination system optimization, Proc. SPIE 5529 (2004) 206–217.
- $\begin{tabular}{ll} [35] & https://ww2.mathworks.cn/help/gads/how-simulated-annealing-works.html. \end{tabular}$
- [36] A. Bauer, S. Vo, K. Parkins, F. Rodriguez, O. Cakmakci, J.P. Rolland, Computational optical distortion correction using a radial basis function-based mapping method, Opt. Express 20 (14) (2012) 14906–14920.
- [37] H. Gross, F. Blechinger, B. Achtner, eds. Handbook of Optical Systems, (WILEY-VCH, 2008), 116.
- [38] R. Kingslake, Illumination in optical images, in Applied Optics and Optical Engineering, II:195, Academic Press, New York, 1965.
- [39] J. Sasín, Introduction to Aberrations in Optical Imaging Systems, Cambridge University Press, (2012) 116.
- [40] M.P. Rimmer, Relative illumination calculations, Proc. SPIE 655 (1986) 99–104.
- [41] Y. Huang, E.L. Hsiang, M.Y. Deng, S.T. Wu, Mini-LED, Micro-LED and OLED displays: present status and future perspectives, Light: Sci. Appl. 9 (1) (2020).
- [42] X. Hu, J.H. Cai, Y.Z. Liu, M.Y. Zhao, E.G. Chen, J. Sun, Q. Yan, T.L. Guo, Design of inclined omni-directional reflector for sidewall-emission-free micro-scale lightemitting diodes, Optics Laser Technol. 154 (2022), 108335.
- [43] Y. Liu, T. Xia, A. Du, T. Liang, Z. Fan, E. Chen, J. Sun, Q. Yan, T. Guo, Omnidirectional color shift suppression of full-color micro-LED displays with enhanced light extraction efficiency, Opt. Lett. 48 (7) (2023) 1650.